

The Dual Nature of Body-Axis Formation in *Hydra* Regeneration: Polarity-Morphology Concurrency

Oded Agam¹ and Erez Braun²

¹The Racah Institute of Physics, Edmond J. Safra Campus, The Hebrew University of Jerusalem, Jerusalem 9190401, Israel.

² Department of Physics and Network Biology Research Laboratories, Technion-Israel Institute of Technology, Haifa 32000, Israel.

ABSTRACT

The formation of a body-axis is central to animal development and involves both polarity and morphology. While polarity is traditionally associated with biochemical patterning, the morphological aspect of axis formation remains elusive. In regenerating *Hydra* tissues, we find that morphological evolution in all tissue samples depends on inherited positional information from the donor's axis, and a foot precursor emerges early in the process. The Ca²⁺ excitations that drive actomyosin forces for tissue reshaping follow a polarity-aligned gradient from the onset of regeneration. We conclude that polarity and morphological axis progression occur concurrently through interlinked processes, and that the foot plays a dominant role in this process, a role usually attributed to the head organizer. These insights from *Hydra* likely extend to broader developmental systems.

Morphogenesis in animal development arises from a complex interplay of biochemical, mechanical, and electrical processes that act across multiple scales, from subcellular dynamics to the whole organism⁽¹⁻¹¹⁾. Identifying the organizational principles that integrate and coordinate these processes for robust developmental outcomes remains challenging. The emergence of a body axis, which provides an organizational skeleton for development, is a prominent manifestation of symmetry-breaking events(12, 13). Yet, the internal anatomical axis may not necessarily mirror external morphological symmetry. In bilaterians, for example, the left-right (LR) axis specifies internal asymmetries despite bilateral external symmetry(14, 15). Thus, axis formation encompasses two processes: polarity, manifested by symmetry-breaking gradients driven by biochemical signals that provide positional cues, and morphological evolution, which shapes the body form. Traditional studies emphasize polarity, but mechanical processes, which are vital for morphological-axis formation, remain less understood(2, 16, 17). These two aspects of the body-axis, polarity and morphology, must be integrated to ensure coordinated animal development(18).

Here, we address this integration using whole-body *Hydra* regeneration from tissue fragments. *Hydra*, a freshwater cnidarian with a single well-defined axis, exhibits robust morphogenesis and remarkable regenerative capacity(4, 9, 19-23). When a flat tissue fragment of several hundred cells is excised from a mature *Hydra*, it first folds into a closed hollow sphere before regenerating into a complete animal(4). Regeneration primarily involves changes in cell shape, tissue reorganization, and differentiation, whereas cell division is not strictly required(22, 24, 25). The head organizer in *Hydra* is considered to play an important role in establishing and maintaining polarity during regeneration, as well as during the continuous developmental process of a mature animal that never ceases (19, 26-29). When a mature *Hydra* is bisected or a tissue fragment is excised, the resulting polarity vector (deduced indirectly by transplantation and grafting experiments) is inherited from the parent animal (30-34). Also, the regeneration dynamics of excised tissue segments and their induction effects when transplanted show traces of “positional” memory of their original location relative to the head organizer along the parent *Hydra*’s axis(26, 35). These observations highlight the head organizer’s role in axis polarity, with the *Wnt/β-catenin* signaling as a key player and *Wnt3* serving as the main inductive signal(27, 28, 33, 34, 36-38).

The primary morphological transition in *Hydra* regeneration, from a spherical shape to a tube-like form, marks the emergence of a morphological axis(8). The *Hydra*’s body behaves like a soft muscle due to supracellular actin fibers in the epithelium(23, 39-41). On the timescale of the morphological transition, shape changes are mainly driven by active contractile forces generated by the actomyosin fibers(4) and by hydrostatic pressure within the tissue’s cavity, modulated by osmotic gradients(34, 42, 43). Although in a tissue fragment, partial actin-fiber alignment is inherited from the parent polyp(4, 23), the distribution of mechanical forces depends on the local concentration of active myosin and Ca^{2+} excitations. Indeed, our previous work shows that Ca^{2+} activity, coupled to tissue curvature, is more influential in determining morphology than mere actin-fiber alignment(8, 44). Further experimental studies demonstrate that the actin fiber organization can adapt to biochemical or mechanical constraints(43, 45), suggesting that these fibers might actually follow, rather than define, the emerging axis.

The main goal of this study is to shed light on morphological-axis formation and gain insight into the question of whether morphology and polarity are two facets of the same process underlying body-axis establishment, or two interdependent processes that proceed in parallel. Towards this goal, we examine the trajectories of various tissue samples in morphological space, each with distinct initial conditions defined by the tissue size and its excision site along the parent *Hydra*’s body-axis. Our findings indicate that polarity

establishment and morphological evolution arise from separate, yet interdependent processes that progress concurrently. In addition, Ca^{2+} excitations, which are critical regulators of morphological changes, show a clear continuous gradient profile, from the onset of a folded excised tissue fragment, which is aligned with the polarity vector. Thus, the Ca^{2+} field serves to integrate polarity and morphological axis formation into a robust regeneration process.

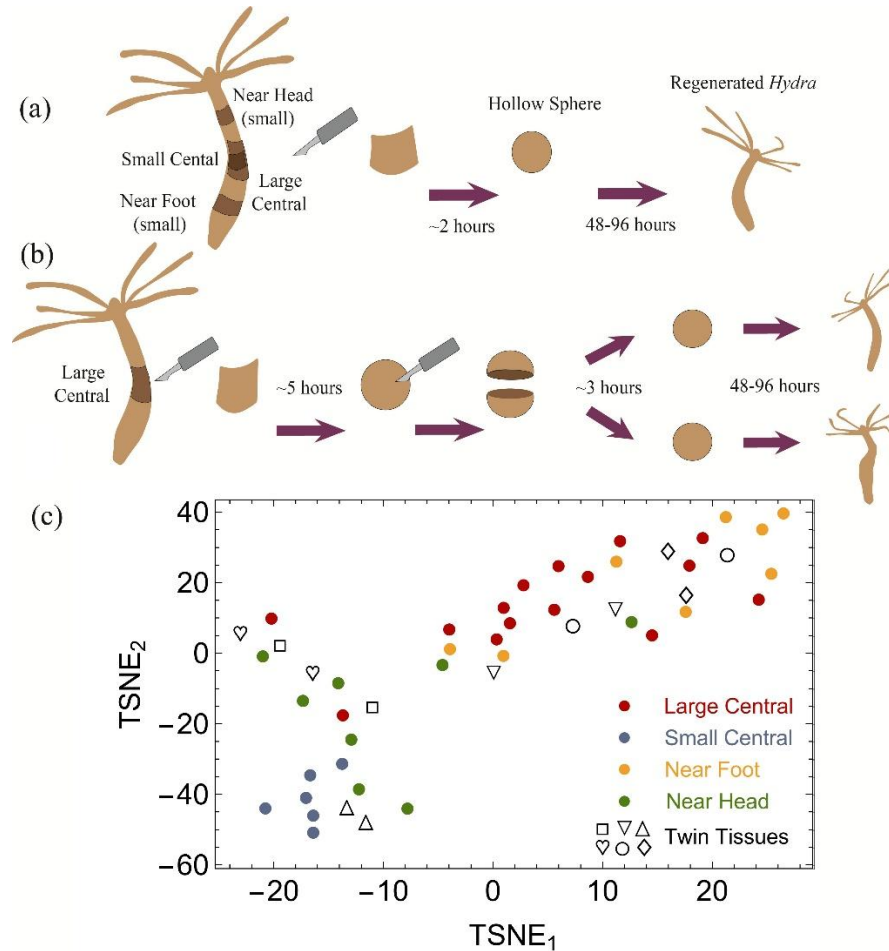


Fig. 1. Experimental protocols and corresponding morphological evolution classification. (a) The experimental procedures used to establish different initial conditions for regenerating tissue samples, accounting for both positional and size dependencies. Tissue fragments typically fold into closed hollow spheres within approximately 2-3 hours after excision, and full regeneration occurs within 48–96 hours. After folding, each tissue fragment is transferred to the experimental setup under a time-lapse fluorescence microscope(8-10, 44). All experiments use the same *Hydra* medium(4), capturing both bright-field (BF) and fluorescence images at one-minute intervals throughout the regeneration process (Methods). (b) Twin tissue experiments: A large tissue fragment excised from the central-axis region of a mature *Hydra*, is allowed to fold into a closed hollow sphere for ~5 hours, after which it is cut into two smaller fragments that re-fold and proceed independently toward regeneration. (c) t-SNE(46) analysis of regeneration trajectories in morphological space for 49 tissue samples, each marked by a dot, revealing clear clustering of tissues based on their initial conditions. Samples: (red) Large tissue samples originated from the central section along the axis of a mature *Hydra*; (blue) small tissue samples excised from the center; (yellow) small tissue samples excised from regions close to the foot; (green) small tissue samples excised from regions close to the head. Black symbols denote twin tissue pairs, with matching symbols indicating samples derived from the same parent tissue fragment. Note that a twin pair is generally positioned close to each other in the reduced space, manifesting their shared characteristics.

Initial Conditions Shape Morphological Dynamics

We first analyze the trajectories of regenerating tissue fragments in morphological space, each defined by different initial conditions (Fig. 1a). For a concise overview of how tissues evolve morphologically under these varying conditions, we apply a t-distributed Stochastic Neighbor Embedding (t-SNE) dimensionality reduction analysis (Fig. 1c)(46). Each sample's trajectory in morphological space is characterized by the transition duration from a spherical to a cylindrical-like shape, and by the magnitude of shape fluctuations, quantified through the leading harmonic moments of the projected tissue image(47, 48) (Eq. (1), and Supplementary Note 1). The clustering of tissue samples according to their initial conditions indicates that both tissue size and positional information—i.e., memory of the excision site along the parent *Hydra*'s axis—play a dominant role in directing the system's morphological evolution. For details on the dimensional reduction procedure and an alternative approach (UMAP(49)) yielding similar results, see Supplementary Note 2 and Fig. S1.

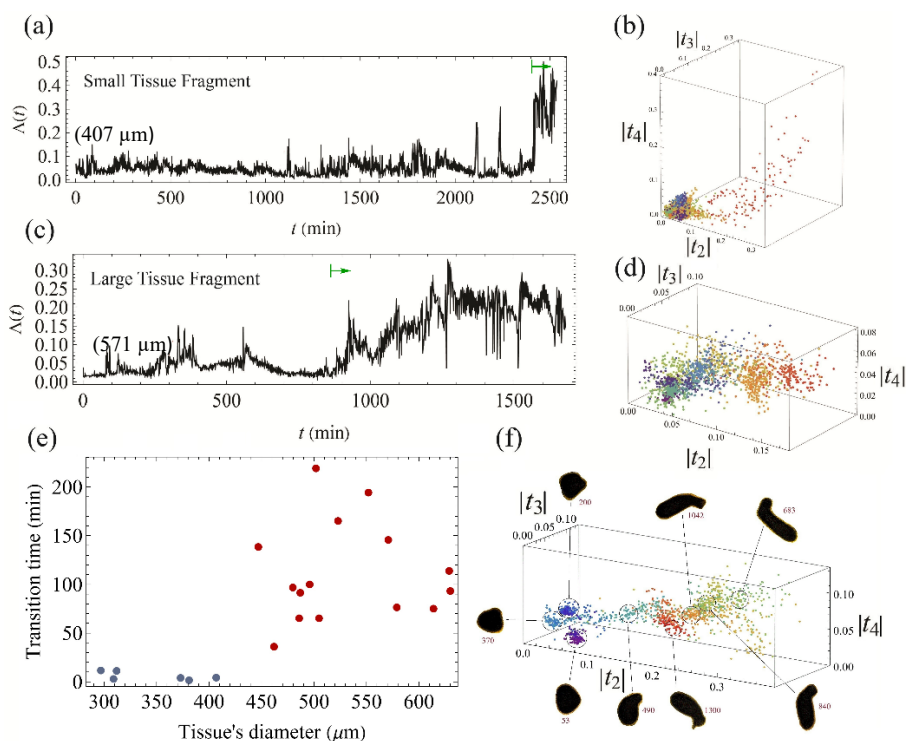


Fig. 2. Morphological evolution of small versus large tissue fragments. (a) Shape parameter evolution of a small tissue fragment excised from the mid-axis of the parent *Hydra*, showing a rapid morphological transition (~ 5 minutes) following an extended period of a nearly spherical shape. (b) Regeneration trajectory of the same small fragment in the reduced morphological space, defined by the absolute values of the leading harmonic moments, with a rainbow color code representing time (purple for early times, red for later stages). (c) Shape parameter evolution of a large tissue fragment excised from the mid-axis of the parent *Hydra*, exhibiting a slow, gradual transition with significant shape fluctuations. The green arrows in panels a and c indicate the onset of the tissue's morphological change, with time in these traces measured from the start of observations, 2–3 hours after excision. (d) Regeneration trajectory of the large fragment in the reduced morphological space. (e) The transition duration of the morphological change as a function of the projected tissue diameter (measured when the fragment is approximately spherical). Blue and red mark small and large central fragments, respectively. (f) A regeneration trajectory of a large tissue fragment in the reduced morphological space, highlighting prolonged residence in quasi-metastable states. Representative tissue images illustrate corresponding morphological states along the trajectory (numbers indicate the respective time of the image).

Quantifying Tissue Shape Dynamics

We next characterize the tissue shape changes over time using a shape parameter, $\Lambda = 1 - 4\pi A/P^2$, where A is the area and P is the perimeter of the projected tissue shape(8, 44). This parameter is zero for a spherical tissue and becomes nonzero whenever the projected image deviates from a perfect circle. During the initial stages of regeneration, the *Hydra*'s body axis typically remains parallel to the imaging plane, deviating out of plane only after the foot is fully developed. Thus, Λ provides a reliable measure of tissue elongation, and its persistent deviation from zero marks the establishment of the morphological axis. However, Λ characterizes only deviations of the projected image from a circular shape, which is insufficient for capturing the full complexity of the tissue's morphology. To address this limitation, we introduce a second measure: the external harmonic moments of the projected *Hydra* image, a method extensively used to describe two-dimensional patterns, defined as(47, 48):

$$t_n = \frac{1}{\pi n} \iint_D \frac{dx dy}{(x + iy)^n}, \quad n = 1, 2, \dots \quad (1)$$

where the domain of integration, D , is the exterior of the projected *Hydra* image. It can be demonstrated that the infinite set of harmonic moments, along with the projected image area, uniquely determine the image shape(47, 48). The first harmonic moment, t_1 , can always be set to zero by appropriately choosing the origin of the coordinate system, a convention we adopt here. All t_n values vanish for a circular domain centered at the origin. For small deviations from a circle, these moments effectively represent the Fourier transform of the polar representation $r(\theta)$ of the projected image contour as a function of the angle θ (Supplementary Note 2). Thus, focusing on the first few moments provides a simplified, coarse-grained description within a reduced-dimensional morphological space.

The Influence of Tissue Size on Morphological Evolution

Fig. 2 illustrates the regeneration dynamics of small and large tissue fragments excised from the central region of the *Hydra*'s axis, using the measures described above. Fig. 2e displays a distinct shift in the morphological transition time for tissue samples exceeding a diameter of $\sim 430 \mu\text{m}$. Below this scale, the morphological transition from a nearly spherical shape to a tubular structure occurs rapidly, typically within a few minutes (Fig. 2a). In contrast, large tissue samples (diameter $> 450 \mu\text{m}$) exhibit a dramatically different behavior, characterized by three key features: (i) a gradual and prolonged morphological transition (Fig. 2c), (ii) broader and more diverse morphological fluctuations (compare Fig. 2b and 2d), and (iii) a regeneration trajectory that traverses a wider range of morphologies, absent in smaller samples (Fig. 2f). These observations were consistently reproduced across 6 independent small samples(8) and 15 large samples, collected from 5 separate experiments (see Supplementary Figures S2 & S3).

Positional Dependence of Morphogenesis

To assess whether the tissue size is the primary factor influencing morphological dynamics, we conduct a "twin-tissue experiment", see Fig. 1b. A large tissue fragment ($> 450 \mu\text{m}$) is excised from the central region of a mature *Hydra* and allowed to fold into a hollow closed spherical shape over approximately 5 hours. The folded tissue is then cut into two sub-fragments, each smaller than the critical-size threshold identified

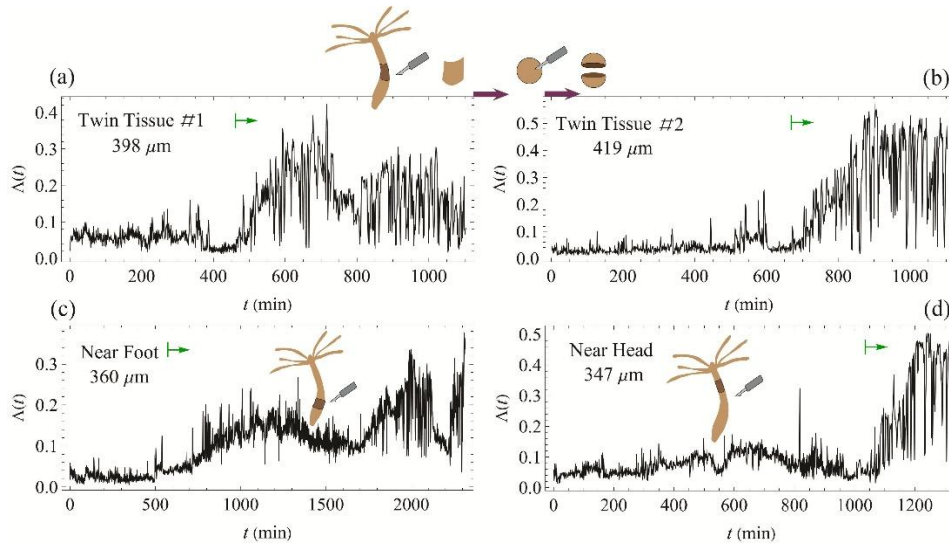


Fig. 3. Impact of positional information on morphological evolution. (a) & (b) Shape parameters over time for a pair of small twin tissue samples, exhibiting gradual morphological transitions accompanied by strong fluctuations. (c) & (d) Shape parameter evolution for small tissue samples excised near the foot and near the head, respectively, demonstrating distinct behaviors compared to small fragments from the central body region, as shown in Fig. 2a. All tissue samples are below the critical size threshold identified in Fig. 2e. Tissue size is measured after folding into hollow spheres and reflects a balance between internal hydrostatic pressure and actomyosin forces; thus, twin tissues are typically larger than half the size of the original parent fragment. Time zero corresponds to the start of measurements, 2–3 hours after cutting (either from the large, folded tissue for twins, or directly from the parent *Hydra* near the head or foot). Green arrows indicate the onset of the tissue’s morphological change.

in Fig. 2e. These smaller sub-fragments are subsequently permitted to re-fold into closed hollow spheres for roughly 3 hours, after which their regeneration trajectories are recorded.

Figs. 3a and 3b show the shape parameter as a function of time for a representative pair of twin tissue samples. The results are striking. Although both samples are below the critical size threshold, their behavior differs significantly from that of small tissue fragments excised directly from the *Hydra*’s mid-axis. Similar patterns were observed across six pairs of twin tissue samples (see Supplementary Fig. S4). These results indicate that the tissue’s size is not the primary factor affecting the regeneration dynamics. Instead, the dynamics are governed by factors inherited from the parent *Hydra*, which are stably transmitted through the large tissue segment to the twin sub-tissue samples derived from it. This inheritance is further supported by the dimensionality reduction analysis presented in the t-SNE map (Fig. 1c, black symbols). The ratio of the average distance between a pair of twin tissue samples (black symbols) to the average distance between non-twin tissues is approximately 0.4, indicating that twin samples typically follow trajectories in morphological space that share similar characteristics. This finding further supports the conclusion that the initial conditions of the tissue, influenced by factors inherited from the parent *Hydra*, significantly affect the regeneration trajectory in morphological space. Moreover, although all twin tissue fragments are below the critical size defined in Fig. 2e, their morphological trajectories generally differ from those of tissue fragments excised directly from the central gastric region of the parent *Hydra*. This suggests that the large parent tissue transmits inherited factors to its twin offspring which play a dominant role in shaping their morphological dynamics. The transmission of inherited attributes is likely due to the broader section of the

parent *Hydra*'s axis encompassed by the large tissue fragment, resulting in a higher concentration of certain factors. This, in turn, suggests that a tissue's trajectory in morphological space is influenced by its original position along the parent body axis. Indeed, as shown in Figs. 3c and 3d, small tissue segments (<450 μm) excised near the head or foot (8 samples each) of the donor *Hydra*, exhibit morphological transitions with characteristics distinctly different from those of segments taken from the mid-axis (Supplementary Figs. S5 and S6)(8).

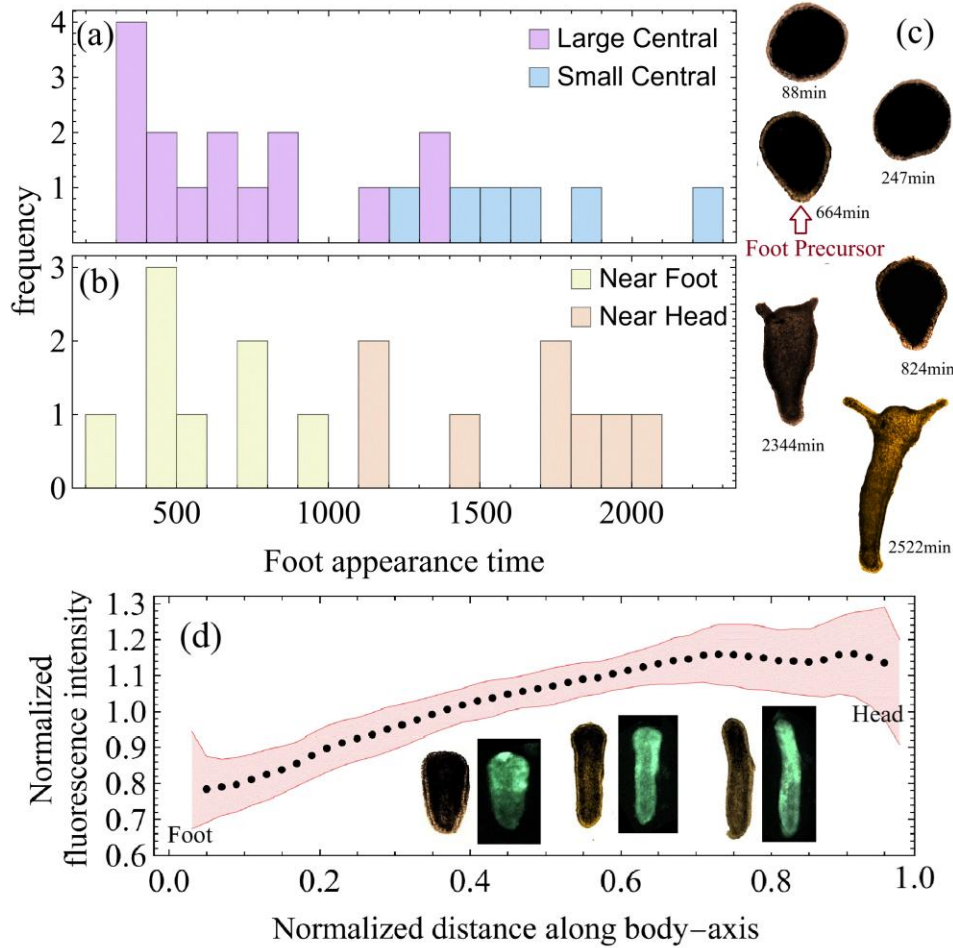


Fig. 4. Indicators of polarity establishment. (a) & (b) Histograms of the approximate appearance time of the foot precursor for large and small mid-axis tissues, as well as small tissues near the head and foot, respectively (time is measured from the tissue's cutting moment). Due to the limitations in analyzing projected tissue images, the observed time represents an upper limit for the first appearance of the foot precursor. (c) Bright-field (BF) images of a regenerating tissue showing the foot precursor indicated by a red arrow. (d) The average normalized fluorescence intensity along the tissue's morphological axis marked by the foot precursor, as a function of normalized distance from the edge (0 = foot, 1 = head). Averaging is done over ~300 consecutive frames around the morphological transition, and the fluorescence levels are normalized by the maximal value in each frame. The distance from the edge is normalized by the tissue's size and accumulated in 50 equal bins. The dots represent the mean values across 11 tissue samples where the foot precursor marking the morphological axis is clearly identified. The pink-shaded region indicates the standard deviation. See Methods for details. Inset: Examples of BF and fluorescence images showing progressively increasing Ca^{2+} activity along the axis from the foot to the head.

Polarity Establishment and Inherited Calcium-Based Polarity Vector

A clear indicator of polarity establishment in a regenerating tissue fragment is the early emergence of a foot precursor, which always appears in our experiments before the primary morphological transition into an elongated tube-like shape (Fig. 4c; Supplementary Figs. S2-S6). The tissue's size and its position along the donor *Hydra*'s body are critical factors in determining the timing of polarity establishment via the appearance of a foot precursor. Figs. 4a and 4b present histograms of the approximate upper-limit times for the appearance of the foot precursor for different sample types, showing a clear hierarchy (see also the traces in Supplementary Figs. S2-S3 and S5-S6); short times for mid-axis large tissue fragments (600 ± 300 min) and small tissue fragments excised near the original foot (1000 ± 550 min), and longer times for mid-axis small fragments (1700 ± 500 min) and for those excised near the original head (1700 ± 300 min). These time differences are aligned with the data shown in the t-SNE map in Fig. 1c.

The timing of foot appearance is also reflected in the distinct morphological trajectories of the tissue fragments (Figs. 2 & 3). It hints that the processes leading to polarity establishment and morphology are interconnected. Our previous studies have highlighted the critical role of Ca^{2+} in driving morphological transitions during *Hydra* regeneration, suggesting that Ca^{2+} may serve as the integrator of these two processes (8, 44). Utilizing the early emergence of a foot precursor as a clear reference for the body-axis, we measure the Ca^{2+} activity along it using a fluorescent probe (*8-10*) (for details see Supplementary Note 3). Figure 4d demonstrates that the average Ca^{2+} activity exhibits a clear gradient reflecting the polarity vector; increasing along the axis from the foot precursor towards the future head (see the same trend for individual tissue samples in Supplementary Fig. S7). This trend in the Ca^{2+} activity is clearly observed in the inset images in Fig. 4d.

We next inquire whether such a gradient also exists at earlier stages of the regeneration process, by analyzing the average Ca^{2+} density from the onset within a sampling circle around the tissue's center of mass. The Ca^{2+} density within this circle is estimated at different time points by accumulating the signal in distance bins from 15 distinct pairs of antipodal points on the diameter of the sampling circle and averaging over 50-time frames (50 min). The pair yielding the largest gradient is chosen as a reference polarity axis (see Supplementary Note 3). As shown in Fig. 5b, the fluorescence profiles along diameters away from that associated with the maximal gradient, deviate gradually by first flattening out and eventually flip direction. Remarkably, our data indicate that a clear Ca^{2+} gradient, in all samples, is already present at the earliest observation point (~2-3 hrs post excision), well before any foot precursor is visible. Comparing this early gradient with the polarity axis measured by the alternative method in Fig. 4d, shows that it is consistently aligned with the axis defined by the foot precursor. As far as we know, this is the first time a continuous gradient reflecting polarity, previously inferred only indirectly through grafting experiments, has been directly observed in *Hydra* (32, 43, 50).

Fig. 5c provides an example where the gradient remains almost constant with time, at least until the tissue begins to elongate significantly, suggesting that the polarity indicated by the Ca^{2+} activity gradient is inherited from the parent *Hydra*. Further support comes from Figure 5d, showing that tissue fragments excised closer to the donor's head display higher initial Ca^{2+} activity than those taken near the foot, consistent with a persistent Ca^{2+} gradient in the adult animal. Over time, however, as the regenerating tissue approaches its main morphological transition, these average Ca^{2+} levels converge toward similar values.

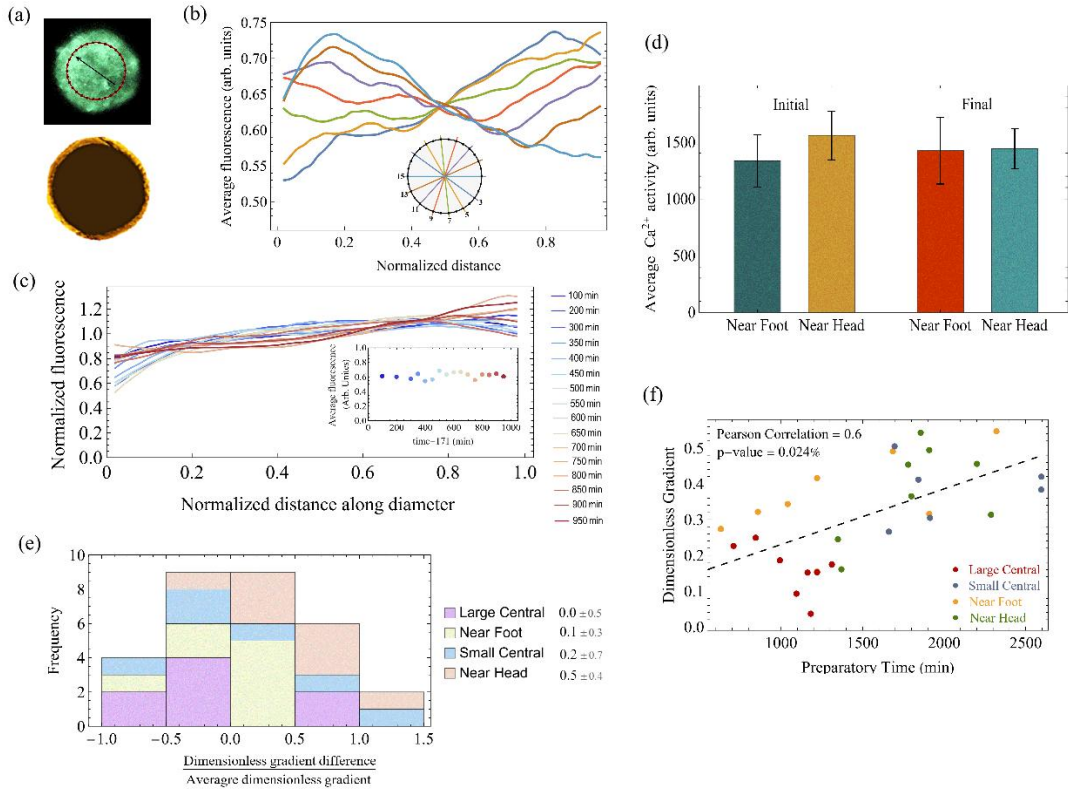


Figure 5. Early Polarity Inheritance and Ca^{2+} Gradient Evolution. (a) Representative BF and fluorescence images of a tissue fragment. The fluorescence signal probes the Ca^{2+} activity. A sampling circle (red), centered at the fragment’s center of mass and spanning 70% of its projected size, is used to measure the average fluorescence along diameters connecting antipodal vertices (30 total; Supplementary Note 3). The arrow indicates the Ca^{2+} gradient direction deduced from the analysis in (c). (b) Example fluorescence profiles measured along 7 representative diameters. Each profile results from averaging over 50 frames (50 min). The antipodal vertices with the largest absolute gradient define the axis. (c) Normalized Ca^{2+} distributions (mean=1) at 16 time points during the “preparatory” interval—the time period prior to the morphological transition. The analysis is done as in (b), and the distribution presented at each time point, marked at the color legend (representing an average over 50 frames at the time point), is the one showing the maximal gradient (the marked time is from the onset of measurement, 2-3 hrs post excision). The measured Ca^{2+} density exhibits a persistent gradient that emerges very early following the folding of the tissue fragment, indicating inherited polarity that is imprinted from the onset in the Ca^{2+} signal. The inset shows the average fluorescence versus time over the same interval. (d) A comparison of mean Ca^{2+} activity in near-foot and near-head samples at the beginning (“initial”) and end (“final”) of the preparatory period. (e) A stacked histogram of the change in dimensionless gradient (from initial to final), normalized by its average value during the “preparatory time”. Different colors correspond to distinct initial conditions. The dimensionless Ca^{2+} gradient is defined as $L(\overline{\partial\rho/\partial x})/\bar{\rho}$, where $\rho(x)$ is the Ca^{2+} density along the identified polar axis, overbar denotes a spatial average, and L is the characteristic tissue size. (f) A scatter plot of the final dimensionless gradient against the “preparatory time”, revealing a positive correlation (Pearson coefficient = 0.6; p = 0.024%).

While Fig. 5c shows a remarkable stability over time, both in the Ca^{2+} gradient (main) and in the average Ca^{2+} activity (inset), this is not always the case. Generally, the initial gradient can differ from the one measured near the main morphological transition. Fig. 5e presents a stacked histogram quantifying these gradient changes, grouped by various tissue types. Near-head samples typically exhibit an increase in the

gradient during the “preparatory time”—the time interval before the primary morphological transition, while near-foot and large central tissues remain comparatively stable. Small central fragments also show an increase, though to a lesser degree than near-head pieces. Finally, Fig. 5f demonstrates that the dimensionless gradient near the morphological transition time correlates positively with the duration of the “preparatory time”.

The Multi-Canalized Landscape of Morphogenesis

A useful way to interpret the above experimental findings is to conceptualize morphological evolution as the Langevin dynamics of an overdamped particle moving under the influence of a slowly changing potential—a landscape in the high-dimensional morphological space. Each tissue fragment inherits positional information from its original location along the parent’s body axis, which defines a characteristic trajectory, a “canal”, within the landscape. In this framework, the rapid morphological transition observed in small, mid-center tissue fragments can be viewed as an activation process, a transition over a barrier between two main potential minima: one corresponding to the incipient spherical shape and another, which gradually deepens over time, corresponding to the tube-like form(8, 44). By contrast, large mid-axis fragments and those excised near the foot or head inherit positional cues that guide their trajectories through a more complex morphological landscape. These tissues navigate via multiple, shallower minima, resulting in a gradual morphological change and possibly visiting “metastable states”, rather than a single abrupt crossing between two states. The “twin experiment” highlights this inherited complexity: fragments derived from the same large tissue follow similar paths, demonstrating that initial conditions (positional and mechanical) shape the morphological landscape experienced by the tissue’s regeneration trajectory.

A key aspect of these initial conditions is the inheritance of polarity, reflected in the observed Ca^{2+} gradients at the onset. Interestingly, these gradients show traces of inherited positional information. Near-foot and large mid-axis fragments typically show a relatively stable gradient during the “preparatory” phase, whereas near-head samples exhibit a smaller initial gradient that increases over time. This pattern correlates with the duration of the “preparatory” stage: near-head tissues undergo prolonged underlying processes—perhaps reorganizing existing signals originated from the parent’s head, or waiting for the establishment of foot signals—which delay their major shape change. During that time, the Ca^{2+} gradient increases to higher levels than those seen in near-foot samples or large central tissues, both characterized by a shorter “preparatory” time. The emergence of a foot precursor is likewise tied to these positional cues. Near-foot and large mid-axis fragments generally develop a foot precursor earlier, presumably due to the inherited proper signals from the start, while near-head or smaller mid-axis tissue fragments must first reorganize the necessary polarity-inducing factors—leading to a delayed foot precursor. Still, the timing of foot precursor formation does not strictly dictate the morphological pathway of a tissue fragment; the t-SNE map (Fig. 1c) shows that tissue samples can share similar precursor timings yet differ in their morphological trajectories.

Our findings paint a picture of *Hydra* regeneration as a multi-canalized process, where polarity and morphological-axis formation progress in parallel and rely on each other—reflecting the dual nature of the developmental body axis. Local positional information shapes both a complex morphological landscape and polarity cues. These, in turn, are mirrored and likely influenced by the spatial distribution of the Ca^{2+} activity, which can feed back into the tissue’s mechanical and morphological dynamics. Moreover, our data suggest the presence of two primary signal sources—one near the head and another near the foot—rather than a single axial gradient originating from a single source in the head as often assumed. The integration

of these insights calls for a revision of the conventional view regarding the head organizer and its biochemical signals as the sole determinant of polarity and morphogenesis. Instead, multiple inherited factors across biochemical, mechanical, and electrical domains simultaneously shape the morphological landscape and polarity signals that guide the regeneration process.

Materials and Methods

Experimental Methods

Experiments are carried out with a transgenic strain of *Hydra Vulgaris* (AEP) carrying a GCaMP6s fluorescence probe for Ca²⁺ (see Refs. ¹⁻³ for details of the strain). Animals are cultivated in a *Hydra* culture medium (HM; 1mM NaHCO₃, 1mM CaCl₂, 0.1mM MgCl₂, 0.1mM KCl, 1mM Tris-HCl pH 7.7) at 18°C. The animals are fed every other day with live *Artemia nauplii* and washed after ~4 hours. Experiments are initiated ~24 hours after feeding. Small tissue fragments are excised from different regions along the axis of a mature *Hydra*, close to the head, close to the foot and at the center. A thin ring is first cut from each of these regions and is further cut into (usually) 4 small fragments. These tissue fragments are incubated in a dish for ~3 hrs to allow their folding into spheroids prior to transferring them to the experimental sample holder. Large tissue fragments are prepared by first cutting a wide ring from the central region of a mature *Hydra*, and then further cutting it into two large fragments. These tissue fragments are incubated in a dish for ~4-5 hrs to allow their folding into spheroids prior to transferring them into the experimental sample holder. For the twin experiments, large tissue fragments are allowed to fold in the *Hydra* medium for ~5 hrs and then cut again into two segments which are allowed to re-fold for ~3 hrs before being transferred to the experimental sample holder. The twin tissue samples are recorded under the same conditions.

The experimental setup is similar to the one described in Ref¹⁻³ without the external electrodes. In all the experiments, spheroid tissues are placed within wells of ~1.3 mm diameter made in a strip of 2% agarose gel (Sigma) to keep the regenerating *Hydra* in place during time-lapse imaging. The tissue spheroids, even the large ones, are free to move within the wells. The agarose strip, containing 15 wells, is fixed on a transparent plexiglass bar of 1 mm height, anchored to a homemade sample holder. A channel on each side separates the sample wells from the electrodes, allowing medium flow. A peristaltic pump (IPC, Ismatec, Füttererstr, Germany) flows the medium continuously from an external reservoir (replaced at least once every 24 hrs) at a rate of 170 ml/hr into two channels around the samples. The medium covers the entire preparation, and the volume in the bath is kept fixed throughout the experiments by pumping the medium out from 4 holes determining the fluid's height. The continuous medium flow ensures stable environmental conditions. All the experiments are done at room temperature.

Microscopy

Time-lapse bright-field and fluorescence images are taken by a Zeiss Axio-observer microscope (Zeiss, Oberkochen Germany) with a 5× air objective (NA=0.25) and acquired by a CCD camera (Zyla 5.5 sCMOS, Andor, Belfast, Northern Ireland). The sample holder is placed on a movable stage (Marzhauser, Germany), and the entire microscopy system is operated by Micromanager, recording bright-field and fluorescence images at 1-minute intervals. The 1 min resolution is chosen on the one hand to allow long experiments while preventing tissue damage throughout the experiments and, on the other hand, to enable recordings from multiple tissue samples.

Data Analysis

For the analysis, images are reduced to 696x520 pixels (~2.5 μm per pixel) using ImageJ. Masks depicting the projected tissue shape are determined for a time-lapse movie using the bright-field (BF) images by a segmentation algorithm described in ⁴ and a custom code written in Matlab. Shape analysis of regenerating *Hydra*'s tissue is done by representing the projected shape of the tissue by polygonal outlines using the Celltool package developed by Zach Pincus ⁵. The polygons derived from the masks provide a series of (x,y) points corresponding to the tissue's boundary. Each series is resampled to 30 points, which are evenly spaced along the boundary. The fluorescence analysis is done on images reduced to the same size as the bright-field ones (696x520 pixels).

References

1. J. B. A. Green, J. Sharpe, Positional information and reaction-diffusion: two big ideas in developmental biology combine. *Development* **142**, 1203-1211 (2015).
2. E. Braun, K. Keren, Hydra Regeneration: Closing the Loop with Mechanical Processes in Morphogenesis. *BioEssays* **40**, 1700204 (2018).
3. T. Lecuit, P.-F. Lenne, E. Munro, Force generation, transmission, and integration during cell and tissue morphogenesis. *Annual review of cell and developmental biology* **27**, 157-184 (2011).
4. A. Livshits, L. Shani-Zerbib, Y. Maroudas-Sacks, E. Braun, K. Keren, Structural inheritance of the actin cytoskeletal organization determines the body axis in regenerating hydra. *Cell Reports* **18**, 1410-1421 (2017).
5. T. Mammoto, A. Mammoto, D. E. Ingber, Mechanobiology and Developmental Control. *Annual Review of Cell and Developmental Biology* **29**, 27-61 (2013).
6. C. J. Miller, L. A. Davidson, The interplay between cell signaling and mechanics in developmental processes. *Nature Rev. Genetics* **14**, 733-744 (2013).
7. J. Howard, S. W. Grill, J. S. Bois, Turing's next step: the mechanochemical basis of morphogenesis. *Nature Review Molecular Cell Biology* **12**, 392-398 (2011).
8. O. Agam, E. Braun, Hydra morphogenesis as phase-transition dynamics. *EPL* **143**, 27001 (2023).
9. E. Braun, H. Ori, Electric-Induced Reversal of Morphogenesis in Hydra. *Biophysical Journal* **117**, 1514–1523 (2019).
10. O. Agam, E. Braun, Universal Calcium fluctuations in Hydra morphogenesis. *Phys. Biol.* **20**, 066002 (2023).
11. M. Levin, Bioelectric signaling: Reprogrammable circuits underlying embryogenesis, regeneration, and cancer. *Cell* **184**, 1971-1989 (2021).
12. C. Niehrs, E. Zapparoli, H. Lee, 'Three signals - three body axes' as patterning principle in bilaterians. *Cells & Development*, 203944 (2024).
13. H. Inomata, Scaling of pattern formations and morphogen gradients. *Dev. Growth Differ.* **59**, 41-51 (2017).
14. S. Bardhan *et al.*, in *Current Topics in Developmental Biology*. (Academic Press, 2024), vol. 159, pp. 310-342.
15. H. Shiratori, H. Hamada, The left-right axis in the mouse: from origin to morphology. *Development* **133**, 2095-2104 (2006).
16. J. Briscoe, A. Kicheva, The physics of development 100years after D'Arcy Thompson's "On Growth and Form". *Mechanisms of Development* **145**, 26-31 (2017).

17. Y. Maroudas-Sacks, K. Keren, Mechanical Patterning in Animal Morphogenesis. *Annu Rev Cell Dev Biol.* **37**, :469-493. (2021).
18. D. Mesnard, M. Filipe, J. A. Belo, M. Zernicka-Goetz, The anterior-posterior axis emerges respecting the morphology of the mouse embryo that changes and aligns with the uterus before gastrulation. *Curr Biol.* **14**, 184-196 (2004).
19. H. R. Bode, Axial Patterning in Hydra. *Cold Spring Harbor Perspectives in Biology* **a000463**, 1 (2009).
20. P. M. Bode, H. R. Bode, Formation of pattern in regenerating tissue pieces of Hydra attenuata: III. The shaping of the body column. *Developmental biology* **106**, 315-325 (1984).
21. C. Futterer, C. Colombo, F. Julicher, A. Ott, Morphogenetic oscillations during symmetry breaking of regenerating Hydra vulgaris cells. *EPL* **64**, 137 (2003).
22. A. Gierer *et al.*, Regeneration of hydra from reaggregated cells. *Nature/New Biology*, 98-101 (1972).
23. Y. Maroudas-Sacks *et al.*, Topological defects in the nematic order of actin fibres as organization centres of Hydra morphogenesis. *Nature Physics* **17**, 251-259 (2021).
24. S. G. Cummings, H. R. Bode, Head regeneration and polarity reversal in Hydra attenuata can occur in the absence of DNA synthesis. *Wilhelm Roux's archives of developmental biology* **194**, 79-86 (1984).
25. H. D. Park, A. B. Ortmeyer, D. P. Blankenbaker, Cell division during regeneration in Hydra. (1970).
26. H. R. Bode, The head organizer in Hydra. *Int. J. Dev. Biol.* **56**, 473-478 (2012).
27. B. Hobmayer *et al.*, WNT signaling molecules act in axis formation in the diploblastic metazoan Hydra. *NATURE* **407**, 186-189 (2000).
28. Y. Nakamura, C. D. Tsiairis, S. Ozbek, T. W. Holstein, Autoregulatory and repressive inputs localize Hydra Wnt3 to the head organizer. *PNAS* **108**, 9137-9142 (2011).
29. M. C. Vogg, W. Buzgariu, N. S. Suknovic, B. Galliot, Cellular, Metabolic, and Developmental Dimensions of Whole-Body Regeneration in Hydra. *Cold Spring Harb Perspect Biol* **13**, a040725 (2021).
30. L. Shani-Zerbib, L. Garion, Y. Maroudas-Sacks, E. Braun, K. Keren, Canalized Morphogenesis Driven by Inherited Tissue Asymmetries in Hydra Regeneration. *Genes* **13**, 360 (2022).
31. L. C. Javois, P. M. Bode, H. R. Bode, Patterning of the head in hydra as visualized by a monoclonal antibody, II. The initiation and localization of head structures in regenerating pieces of tissue. *Dev Biol.* **129**, 390-399 (1988).
32. H. K. MacWilliams, Hydra transplantation phenomena and the mechanism of hydra head regeneration: II. Properties of the head activation. *Developmental biology* **96**, 239-257 (1983).
33. R. Wang, R. E. Steele, E.-M. S. Collins, Wnt signaling determines body axis polarity in regenerating Hydra tissue fragments. *Developmental Biology* **467**, 88-94 (2020).
34. J. Ferenc *et al.*, Mechanical oscillations orchestrate axial patterning through Wnt activation in Hydra. *Science Advances* **7**, eabj6897 (2021).
35. A. Livshits *et al.*, Plasticity of body axis polarity in Hydra regeneration under constraints. *Scientific Reports* **12**, 13368 (2022).
36. T. W. Holstein, The role of cnidarian developmental biology in unraveling axis formation and Wnt signaling. *Developmental Biology* **487**, 74-98 (2022).

37. S. Gufler *et al.*, β -Catenin acts in a position-independent regeneration response in the simple eumetazoan Hydra. *Developmental Biology* **433**, 310-323 (2018).
38. M. Veschgini *et al.*, Wnt/ β -catenin signaling induces axial elasticity patterns of Hydra extracellular matrix. *iScience* **26**, 106416 (2023).
39. R. Aufschnaiter, R. Wedlich-SÃ, X. Zhang, B. Hobmayer, Apical and basal epitheliomuscular F-actin dynamics during Hydra bud evagination. *Biology Open* **6**, 1137-1148 (2017).
40. M. F. Lefebvre, N. H. Claussen, N. P. Mitchell, H. J. Gustafson, S. J. Streichan, Geometric control of myosin II orientation during axis elongation. *eLife* **12**, e78787 (2023).
41. J. Szymanski, R. Yuste, Mapping the Whole-Body Muscle Activity of Hydra vulgaris. *Current Biology* **29**, 1807-1817 (2019).
42. M. Kucken, J. Soriano, P. A. Pullarkat, A. Ott, E. M. Nicola, An osmoregulatory basis for shape oscillations in regenerating Hydra. *Biophys J* **95**, 978-985 (2008).
43. R. Wang, A. L. Bialas, T. Goel, E. S. Collins, Mechano-Chemical Coupling in Hydra Regeneration and Patterning. *Integr Comp Biol.* 2023 Dec 29;63(6):1422-1441. doi: 10.1093/icb/icad070. **63**, 1422-1441 (2023).
44. O. Agam, E. Braun, Stochastic morphological swings in Hydra regeneration: A manifestation of noisy canalized morphogenesis. *Proceedings of the National Academy of Sciences* **122**, e2415736121 (2025).
45. Y. Maroudas-Sacks, L. Garion, S. Suganthan, M. PopoviÄ, K. Keren, Confinement Modulates Axial Patterning in Regenerating Hydra. *PRX Life* **2**, 043007 (2024).
46. L. J. P. van der Maaten, G. E. Hinton, Visualizing Data Using t-SNE. *Journal of Machine Learning Research* **9**, 2579–2605 (2008).
47. S. Richardson, Hele Shaw flows with a free boundary produced by the injection of fluid into a narrow channel. *Journal of Fluid Mechanics* **56**, 609-618 (1972).
48. M. Mineev-Weinstein, P. B. Wiegmann, A. Zabrodin, Integrable Structure of Interface Dynamics. *Physical Review Letters* **84**, 5106-5109 (2000).
49. J. Healy, L. McInnes, Uniform manifold approximation and projection. *Nature Reviews Methods Primers* **4**, 82 (2024).
50. H. Shimizu, Transplantation analysis of developmental mechanisms in Hydra. *Int. J. Dev. Biol.* **56**, 463-472 (2012).

Acknowledgements:

We thank Omri Gat, Kinneret Keren, Shani Maoz, and Omri Wurtzel for useful discussions and comments on the manuscript. EB thanks Liora Garion for technical help. This work was supported by a grant (EB) from the Israel Science Foundation (Grant No. 1638/21)).

List of Supplementary Materials:

Supplementary Figs. S1 to S7

Supplementary Notes 1-3

References

Supplementary Material for

The Dual Nature of Body-Axis Formation in *Hydra* Regeneration: Polarity-Morphology Concurrency

Oded Agam¹ and Erez Braun²

¹The Racah Institute of Physics, Edmond J. Safra Campus, The Hebrew University of Jerusalem,
Jerusalem 9190401, Israel.

² Department of Physics and Network Biology Research Laboratories, Technion-Israel Institute of
Technology, Haifa 32000, Israel.

This PDF file includes:

Supplementary Figs. S1 to S7

Supplementary Notes 1-3

References

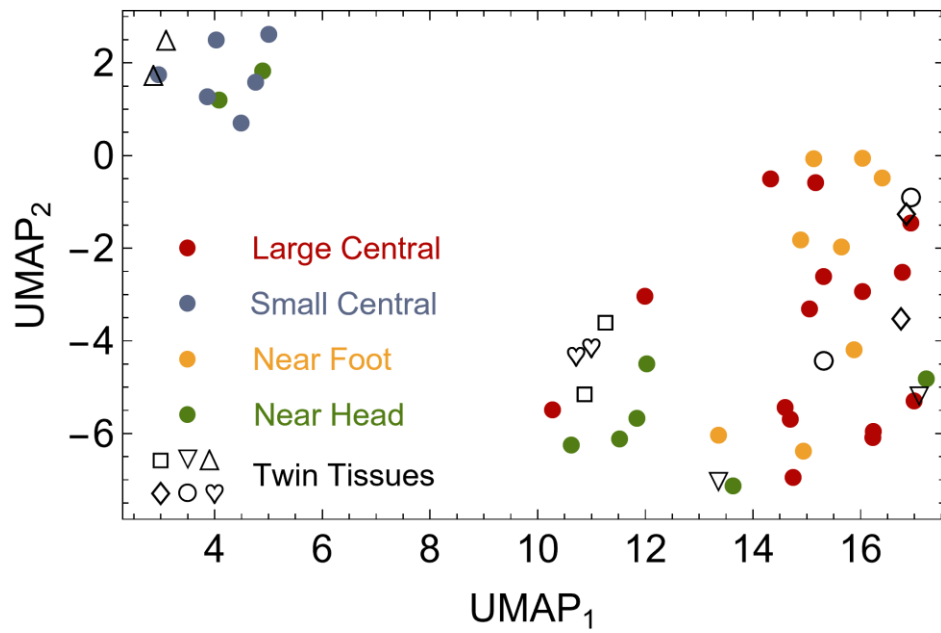


Fig. S1. Dimensionality reduction by UMAP. The same experimental protocols and corresponding morphological evolution classification used in Fig.1, utilizing the UMAP method instead of t-SNE.

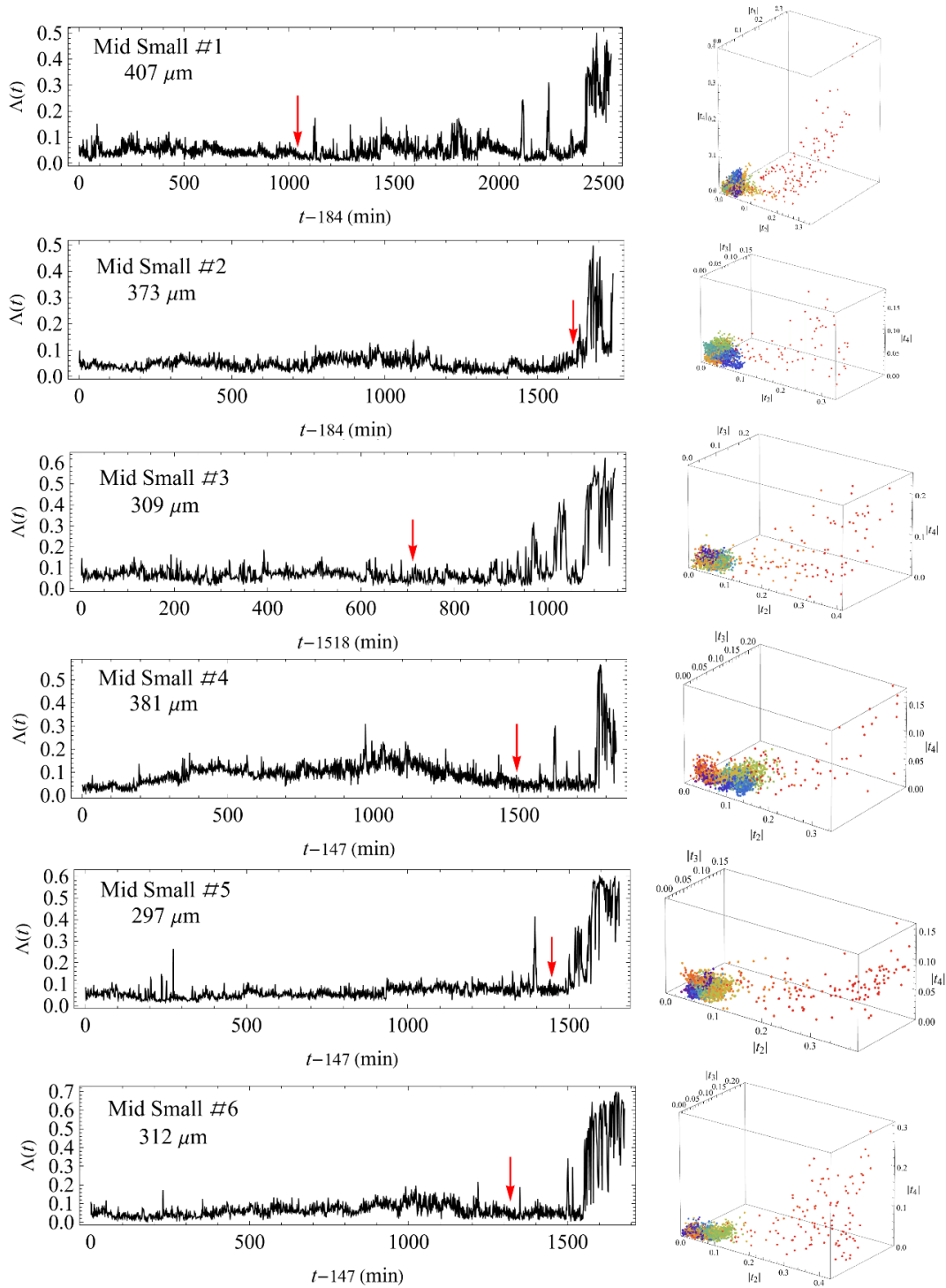


Fig. S2 Time traces and harmonic moments of individual small tissue samples. (Left) The shape parameter traces of individual tissue samples. (Right) The regeneration trajectories in the reduced morphological space, defined by the absolute values of the leading harmonic moments, with a rainbow color code representing time (purple for early times, red for later stages). The data shown is for small tissue samples excised from the mid-axis region of the parent *Hydra*. The red arrows mark the time point of the emergence of a foot precursor that can be identified in the bright-field microscopy images.

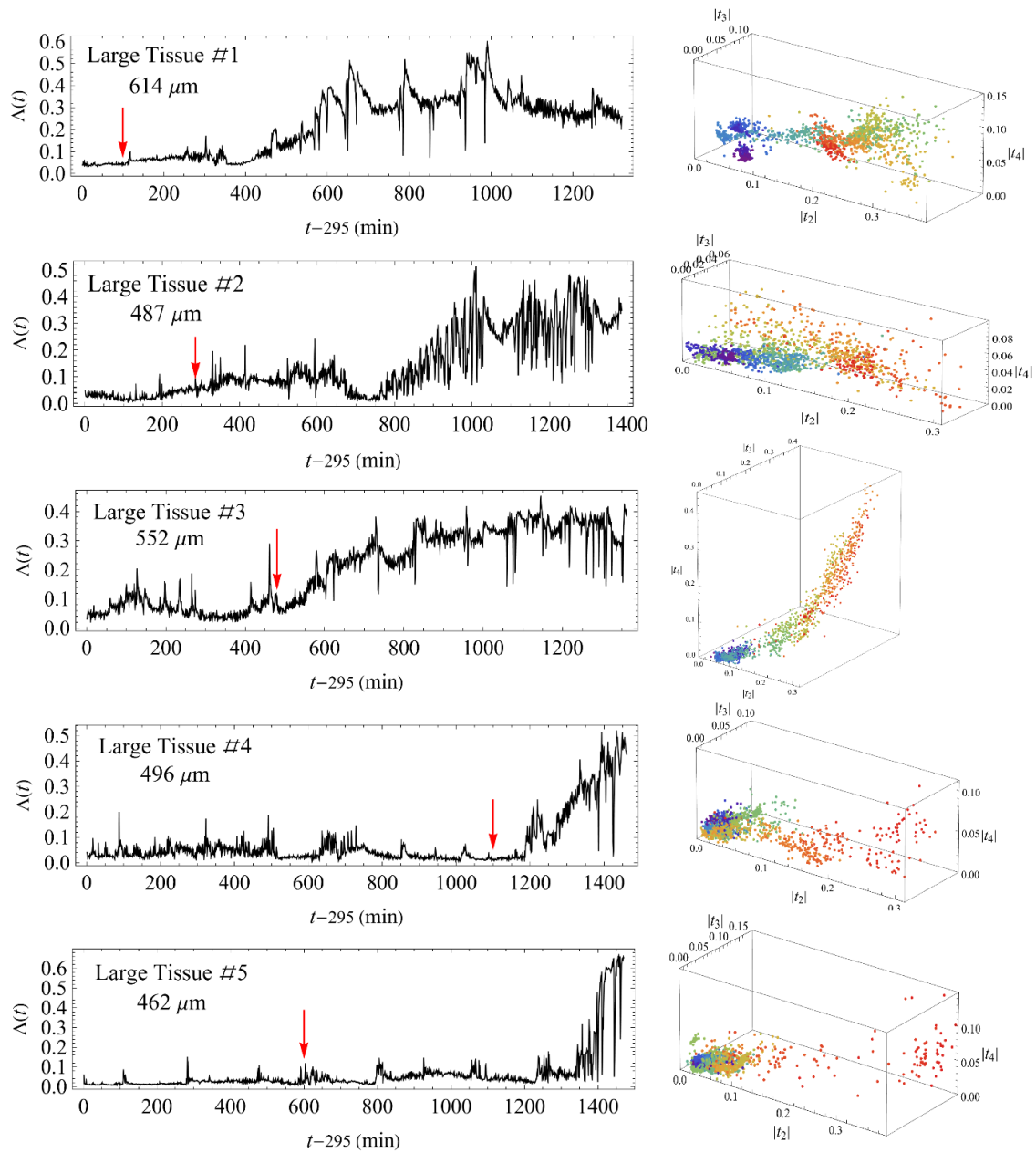


Fig. S3 Time traces and harmonic moments of individual large tissue samples. The same as in Fig. S2 for large tissue samples excised from the mid-axis region of the parent *Hydra*.

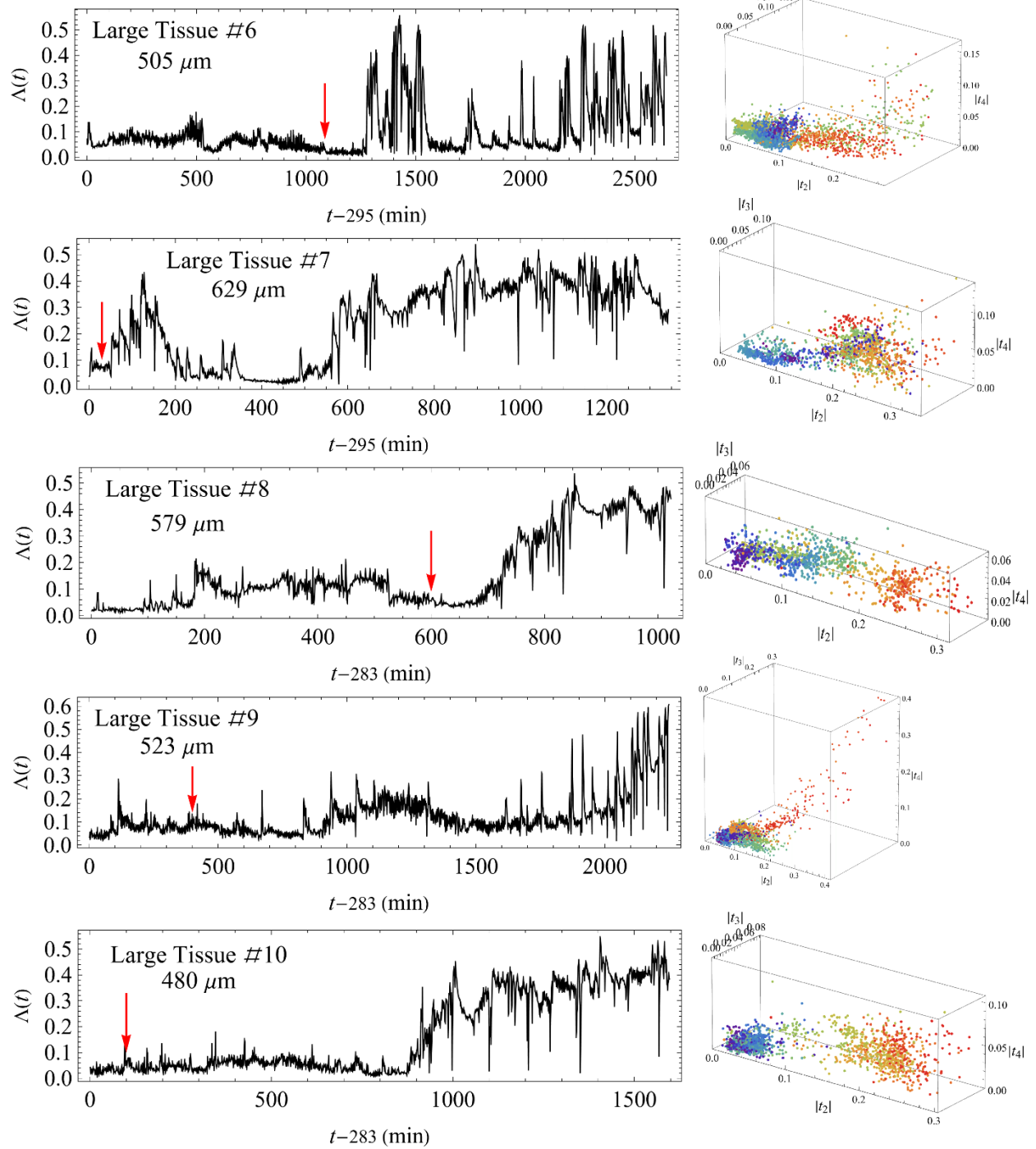


Fig. S3 (Cont.)

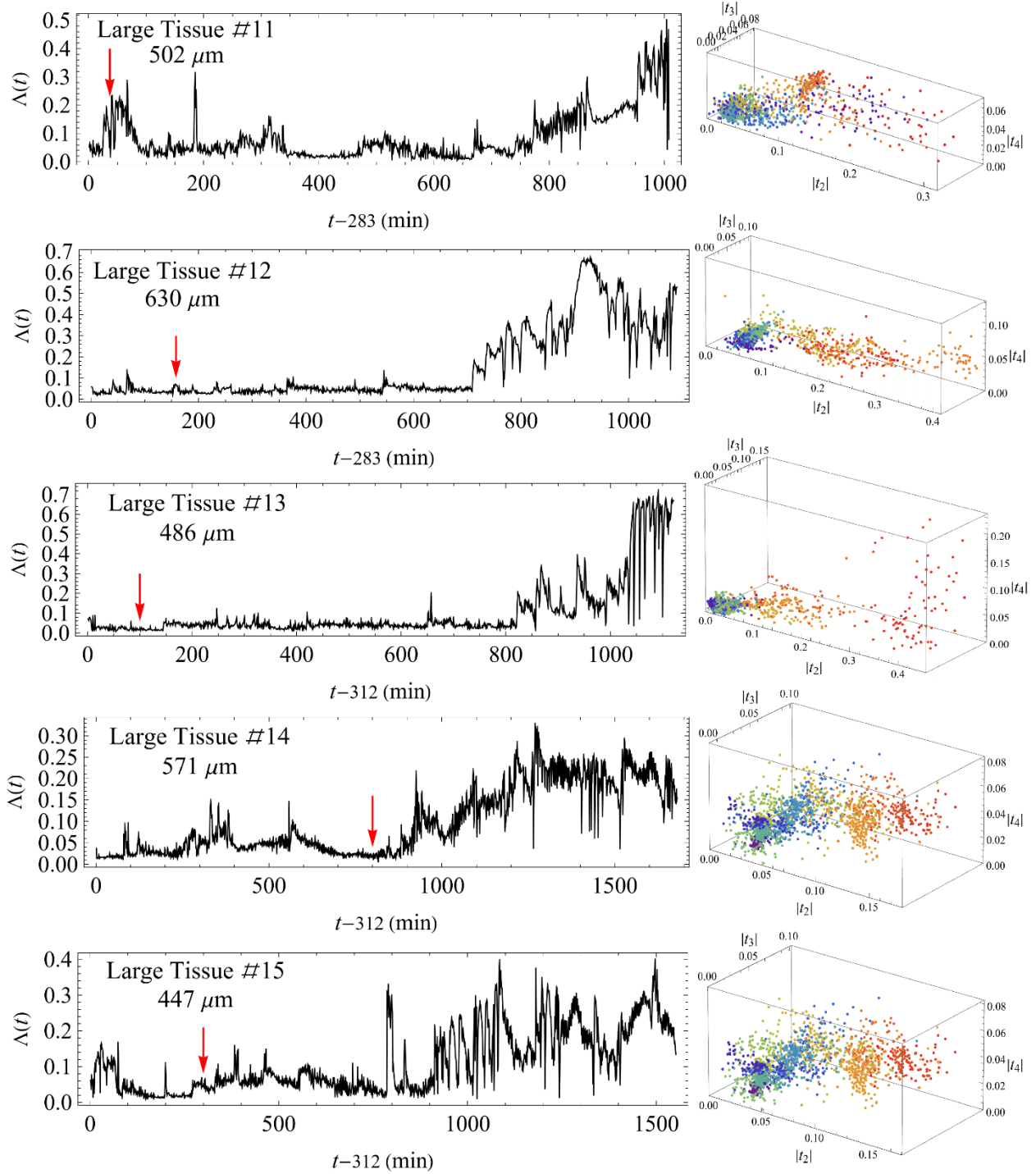


Fig. S3 (Cont.)

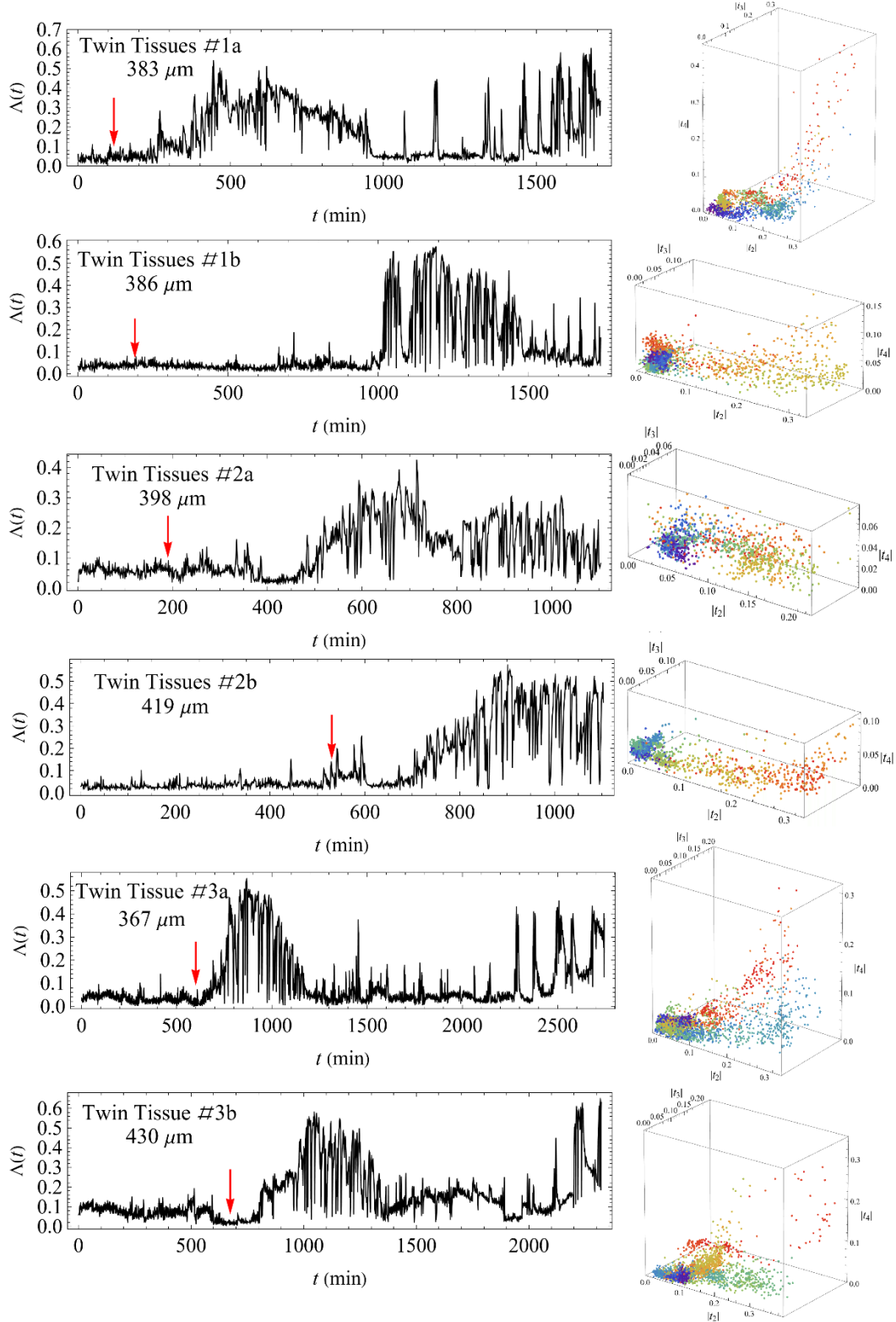


Fig. S4. Time traces and harmonic moments of twin tissue samples. The same as in Fig. S2 for twin samples. Each pair of samples is derived from a single large tissue fragment excised from the mid-axis of the parent *Hydra* (see Methods).

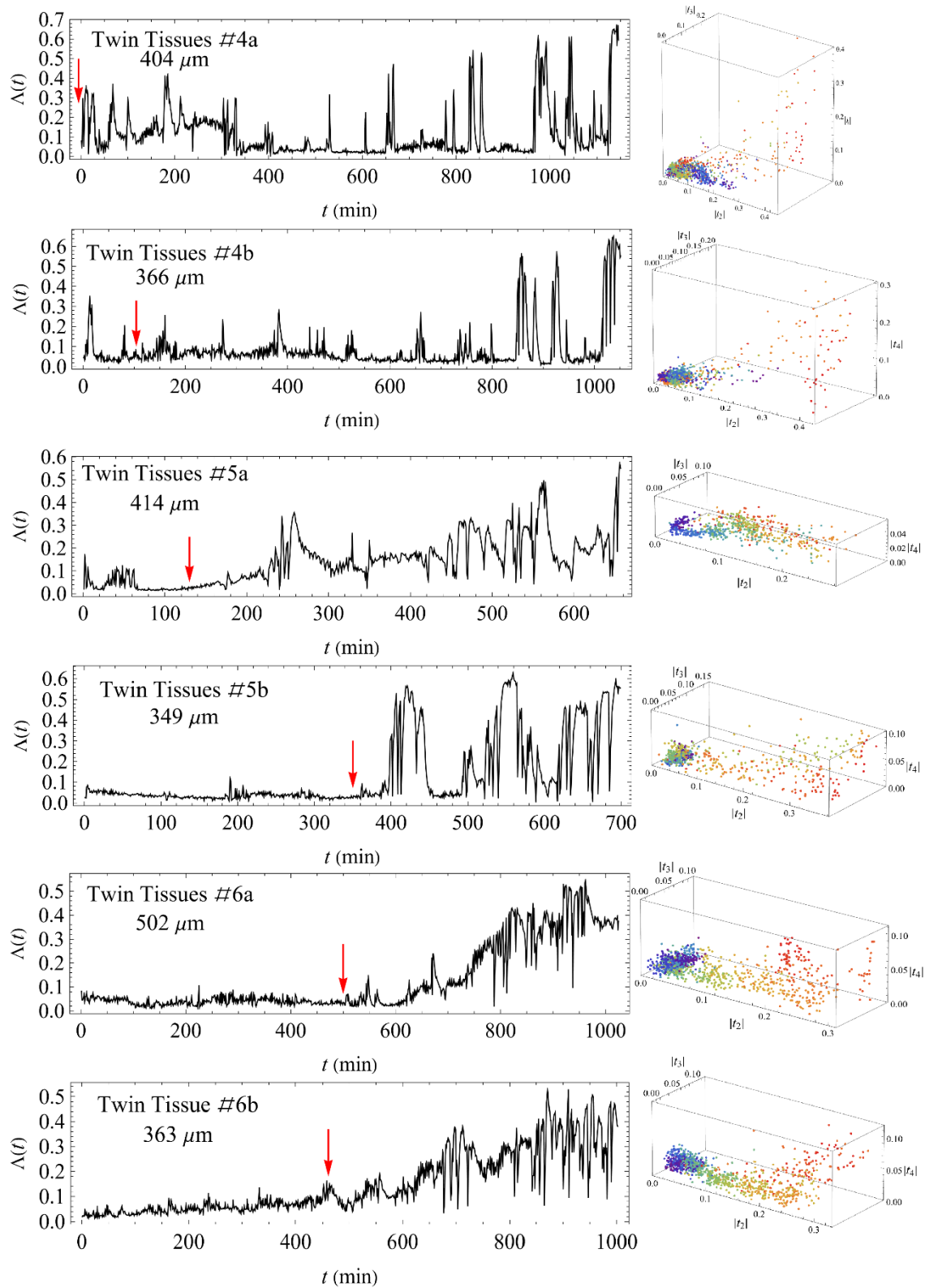


Fig. S4. (Cont.)

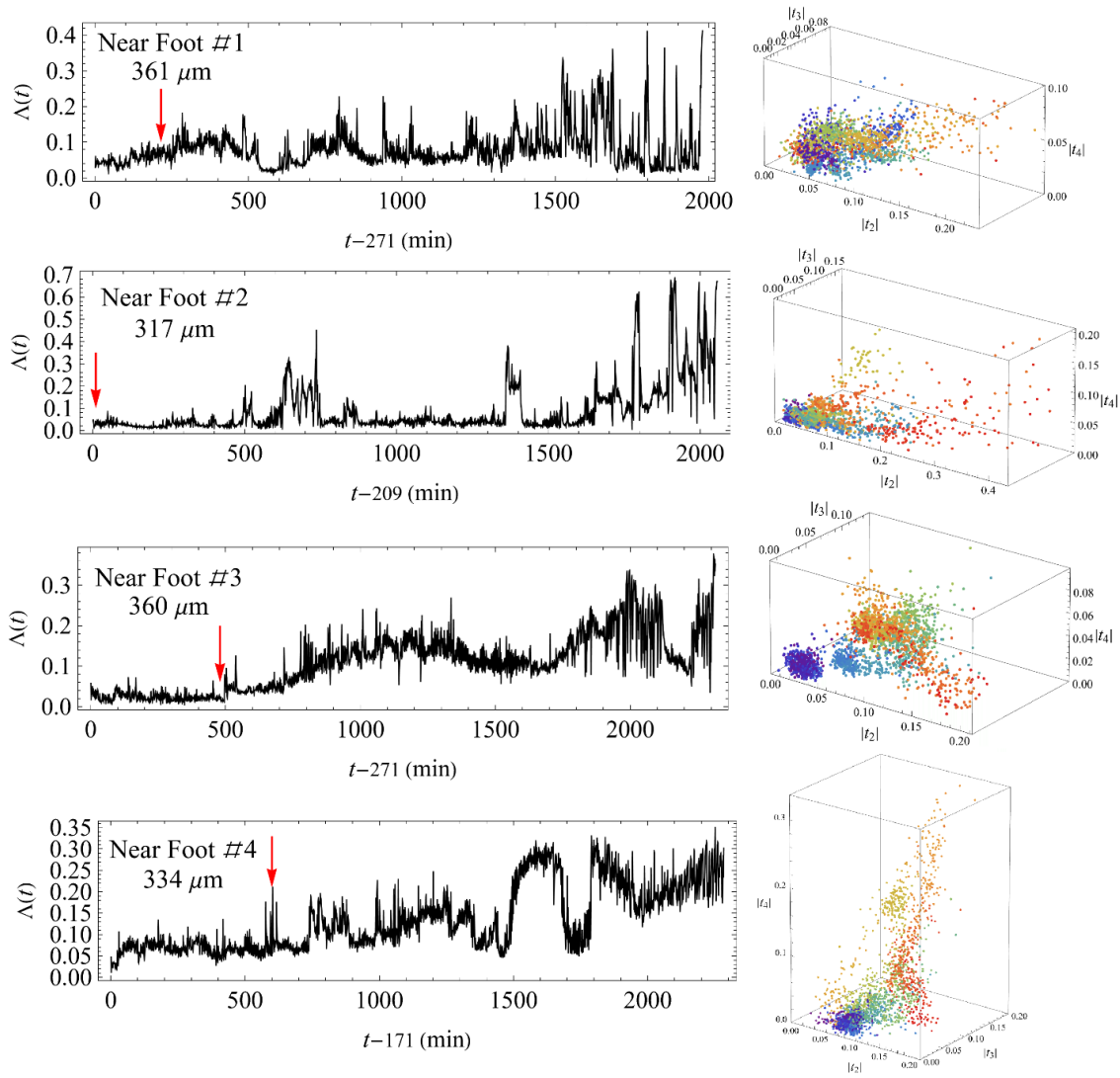


Fig. S5. Time traces and harmonic moments of individual near-foot tissue samples. The same as in Fig. S2 for small tissue samples excised from regions near the foot of the parent *Hydra*.

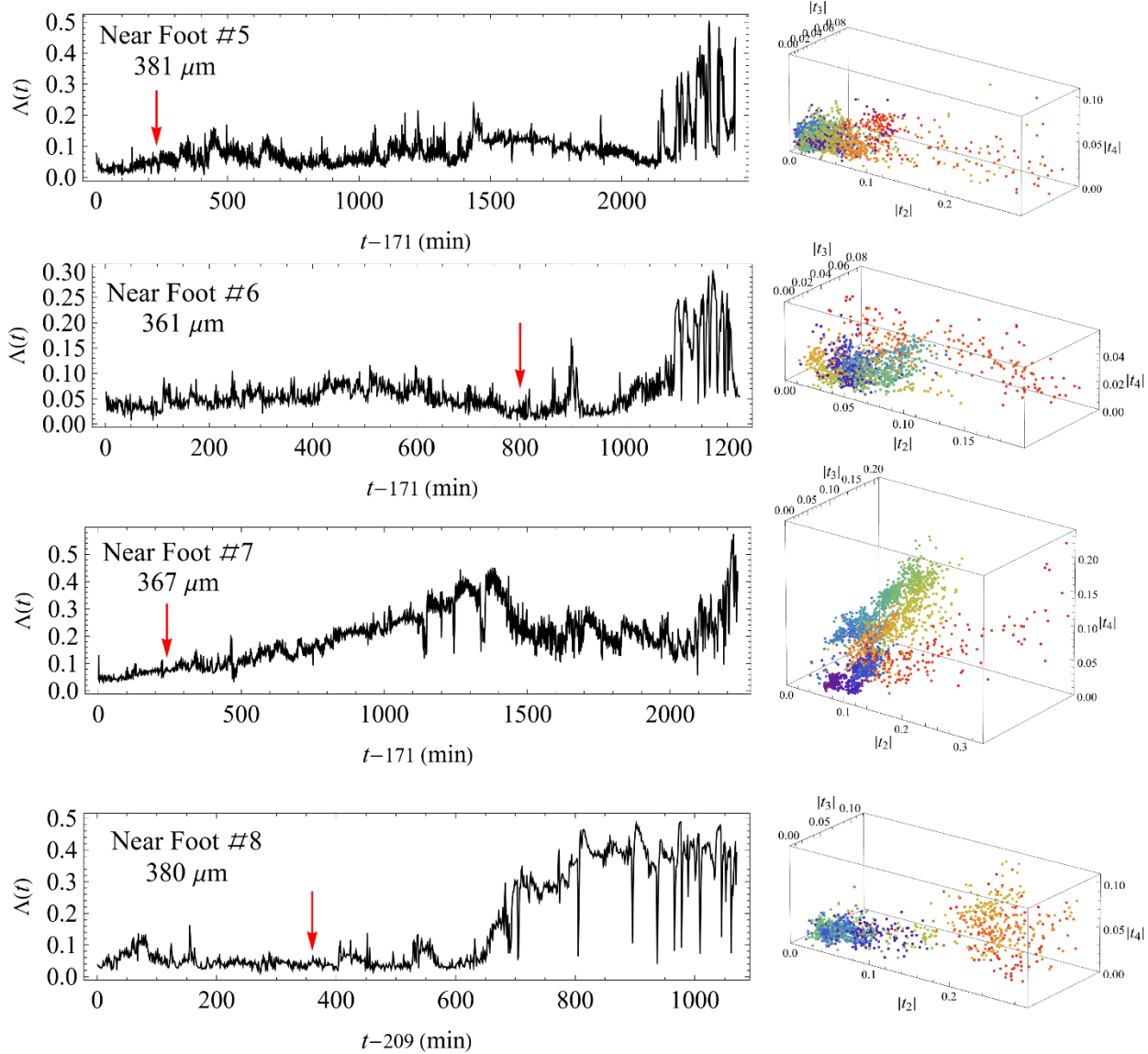


Fig. S5. (Cont.)

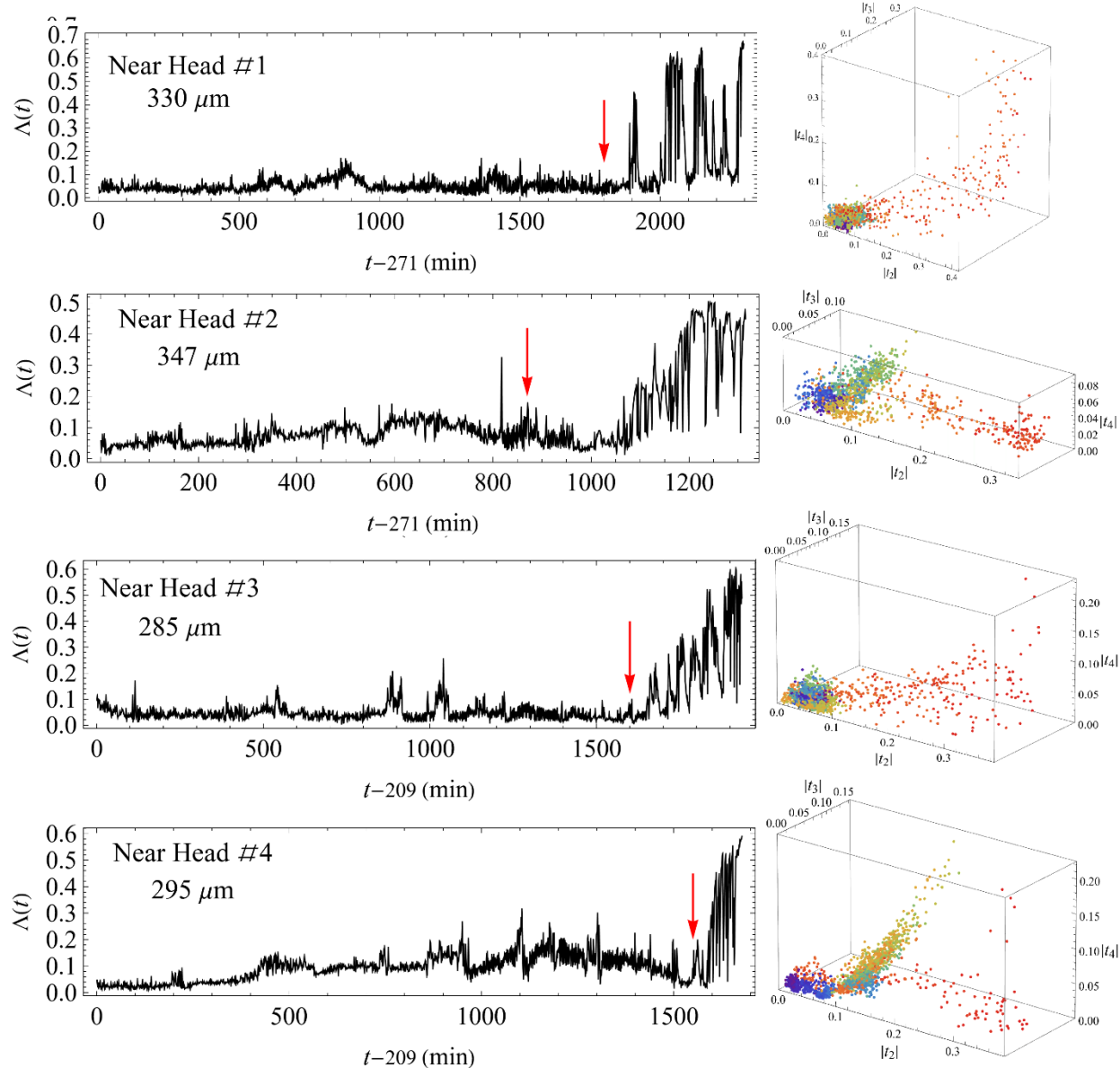


Fig. S6. Time traces and harmonic moments of individual near-head tissue samples. The same as in Fig. S2 for small tissue samples excised from regions near the head of the parent *Hydra*.

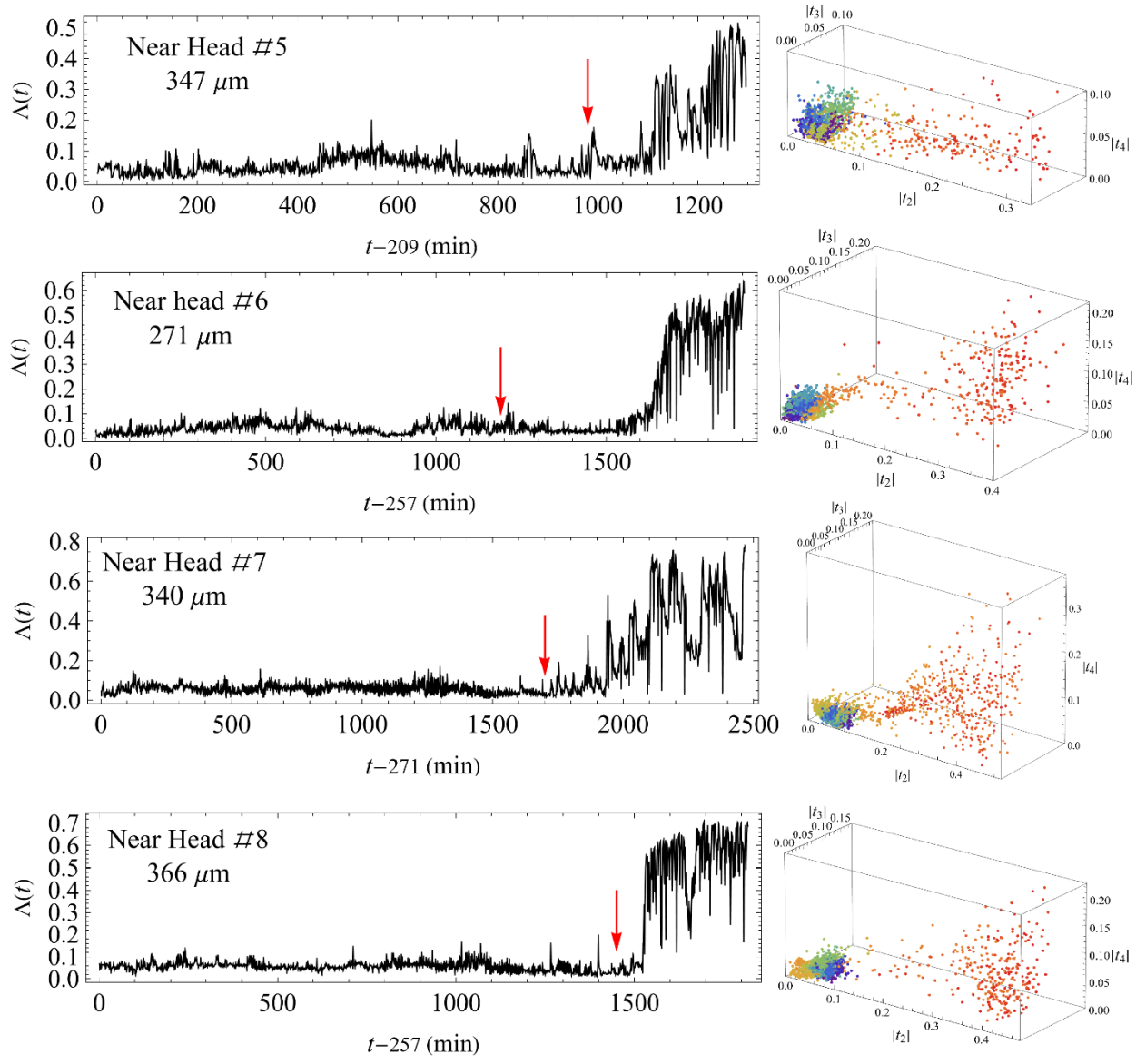


Fig. S6 (Cont.).

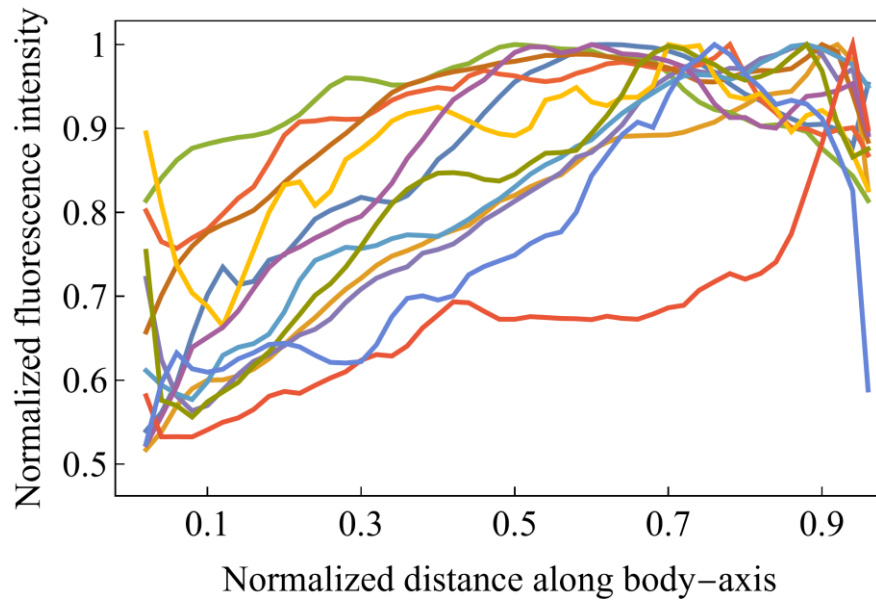


Fig. S7. Normalized Ca^{2+} average activity along the body axis. The figure displays curves of the average fluorescence signal—proportional to Ca^{2+} activity—normalized by its maximum value and plotted against the distance from the foot precursor (also normalized by the total distance). Data from 12 different tissue samples, covering all types of initial conditions, are shown. See Supplementary Note 3 for calculation details.

Supplementary Note 1: Harmonic Moment Analysis for Tissue Morphology

In this note, we describe how the two-dimensional projection of the tissue at any given time can be viewed as a vector in an infinite-dimensional space. The tissue-projected image can be approximated as a closed, non-intersecting curve in a two-dimensional plane. One way to span the morphological space is by using the area enclosed by the curve, along with the external harmonic moments defined in Eq. (1). The area integral for these moments can be converted into a contour integral using Green's theorem:

$$t_n = -\frac{1}{2\pi ni} \oint dz \frac{z^*}{z^n}, \quad n = 1, 2, \dots \quad (\text{S1})$$

where $z = x + iy$ is the complex coordinate in the image plane, $z^* = x - iy$ is its complex conjugate, and the integral is taken along the projected boundary. From the above formula it is evident that all external harmonic moments vanish if the contour is a circle centered at the origin.

For small deviations from a circular shape, t_n is approximately given by the Fourier transform of the contour's polar representation, up to a constant factor. If the enclosed area of the projected *Hydra*'s tissue shape is normalized to π and the contour is described by small distortions of a circle such that its polar representation is given by $r(\theta) = 1 + \delta r(\theta)$ (with $|\delta r(\theta)| \ll 1$), then substituting this representation into Eq. (S1) and expanding to first order in $\delta r(\theta)$ leads to

$$nt_n = \frac{1}{\pi} \int_0^{2\pi} d\theta \delta r(\theta) \exp(-in\theta) = 2\delta r_n^* \quad (\text{S2})$$

Thus, the Fourier coefficients, δr_n , characterize deformations into n -fold symmetric shapes. For instance, $|t_2|$ increases for an elliptical distortion, while $|t_3|$ grows when the contour evolves into a three-petal configuration. The set of harmonic moments, together with the area enclosed by the contour, uniquely define the contour shape. The characterization by harmonic moments is advantageous because it also applies when the polar representation $r(\theta)$ is multivalued and the Fourier coefficients are undefined.

An additional measure of morphology is the shape parameter $\Lambda = 1 - 4\pi A/P^2$, where A is the area and P is the perimeter of the projected tissue (1, 2). For an ellipse of small eccentricity, $\Lambda \approx 6t_2^2$. Yet any type of deviation from a circular shape yields a nonzero Λ .

Supplementary Note 2: Dimensionality Resection Procedures

Tracking t_n over time defines the trajectory of the projected tissue image in the morphological space spanned by the harmonic moments (after area normalization). Since the *Hydra*'s body form is approximately a tube-like structure, and early deformations (before the foot is fully formed) occur primarily parallel to the projection plane, harmonic moments effectively capture the time evolution of its three-dimensional structure.

To characterize these trajectories, four dimensionless parameters are used. The first is the duration of the morphological transition— from a near-spherical to an elongated tube-like shape—normalized by the average transition time across all samples. This duration is extracted by fitting $a + b \tanh\left[\frac{(t - t_*)}{\sigma}\right]$ to $\Lambda(t)$ near the transition region, with a , b , t_* and σ as fitting parameters, and defining σ as the approximate transition duration (I). The remaining three parameters quantify the magnitude of shape fluctuations and are taken as the coefficients of variation (standard deviation over mean) of the absolute values of the first three harmonic moments. These quantify how much the regeneration trajectory meanders in the reduced morphological space spanned by these moments, reflecting the relative time spent in “metastable” states.

Each of the 49 samples in our experiments is thus represented by a four-dimensional vector capturing the main features of its regeneration trajectory. Dimensional reduction is performed first via t-SNE(3) in Mathematica© (perplexity = 12), as shown in Fig. 1, and then via the *Uniform Manifold Approximation and Projection* (UMAP) (4) with Neighbors Number = 14 and Min Distance = 2, illustrated in Fig. S8. Under UMAP, the ratio of the average twin-sample distance to the average non-twin distance is ~ 0.26 . This ratio reduction compared to t-SNE which yields a ratio of ~ 0.4 , results from the more pronounced separation between rapidly transitioning samples and all other samples.

Supplementary Note 3: Computation of the Ca^{2+} Gradient

In the first of the two procedures used to identify and compute the gradient in the Ca^{2+} distribution, we take advantage of the foot precursor to determine the polarity axis. We begin by locating the central point of the foot, labeled A in Fig. S8a, and measure the distance of every pixel in the projected image from point A. The pixels used are the ones within the mask polygon described above (contracted by 10% to prevent edge effects). These distances are grouped into 50 equal bins, and the fluorescence level in each bin is averaged over 300 consecutive time frames (300 min). The pixel fluorescence intensity is normalized by the maximal pixel intensity in each frame, and the pixel distances are normalized by the scale derived from the tissue’s area in each frame. Next, we locate the antipodal point, which is found by drawing a line through point A and the image’s center of mass (point B in Fig. S8a) and identifying the point that intersects the image boundary on the opposite side. We repeat the same binning and averaging for this antipodal point. An example of these two calculations is depicted by the red and blue curves in Fig. S8b. Finally, we flip the direction of the distribution associated with point B and then average the two distributions. The resulting black curve in Fig. S8b represents our final estimate of the Ca^{2+} gradient along the line from A to B.

To verify that this procedure indeed captures the gradient along A–B, we repeat the calculation but restrict the averaging only to pixels within a narrow stripe along the A–B line, as shown in Fig. S8c. The stripe computation repeats the same procedure as above, namely, averaging the two distributions within the stripe computed from both ends. The corresponding results, plotted in Fig. S8d, confirm that within the central region of the stripe ($0.1 < x < 0.9$ where x is the normalized distance from A along the line to B), the two calculations (red for point A and blue for point B) nearly coincide, and they diverge only near the endpoints. Moreover, the overall results of the two calculations (shown by the black curves in Figs. S8b and S8d) are similar in this central region, as highlighted in Fig. S8e.

The second computational procedure identifies and quantifies the gradient of the average Ca^{2+} density prior to the emergence of the foot precursor, when the projected tissue image is approximately circular and the polarity axis is unknown. We define a sampling circle, with 30 equal-distance vertices, around the image's center of mass, with a diameter equal to 70% of the size determined by the minor axis of the tissue, approximated as an ellipsoid (see Figs. 5a & S8f). Then, along 15 vertices of the sampling circle, each separated by an angle $\Delta\theta = \pi/15$, we measure the fluorescence intensity $\rho(x)$ (as a function of distance x along the diameter), averaged over 50 consecutive time frames (50 min), using the above binning approach for points A and B and averaging of the computed fluorescence distribution from both ends. Here, A and B mark the opposite ends of each diameter (antipodal vertices), and only pixels within the sampling circle are included. A 50-frame average is sufficient to reduce the noise levels and is short enough to ensure that the tissue does not undergo significant shape or rotational changes during the measurement.

Next, we fit $\rho(x)$ to a linear function $\rho_{\text{fit}}(x) = \bar{\rho} + \alpha(x - x_0)$, where $\bar{\rho}$ is the average intensity along the diameter, α is a fitting parameter, and x_0 is the center point of the diameter. The parameter α represents the average gradient along that diameter. Figure 5b illustrates typical averaged fluorescence profiles along diameters oriented at different angles. The maximal value of $|\alpha|$ obtained from these fits approximates the Ca^{2+} density gradient (up to a multiplicative constant) along the axis defined by the diameter direction of maximal slope. Accordingly, we define the dimensionless gradient as

$$\text{Dimensionless gradient} = \frac{D}{0.7} \frac{|\alpha|_{\text{max}}}{\bar{\rho}}, \quad (\text{S3})$$

where D is the circle diameter, and $D/0.7$ characterizes the tissue's projected size.

An example of the fluorescence intensity obtained via this procedure is depicted by the blue curve in Fig. S8h. The maximum gradient in that case aligns with the diameter running through the blue cross and the circle's center in Fig. S8f. To verify this method, we repeat the calculation using the stripe geometry in Fig. S8g, producing the brown curve in Fig. S8h. Within the range $0.1 \leq x \leq 0.9$, the gradients from the two profiles differ by approximately 0.3%, confirming the procedure's validity.

In the second procedure, where the foot precursor is not yet observed and the polarity axis is unknown, several factors can potentially distort the computed Ca^{2+} gradient. First, morphological fluctuations and tissue rotation may lead to an underestimation of the gradient. Although we average over 50 consecutive minutes to minimize these effects, the diameters in the sampling circle remain fixed in orientation. Any residual rotation or shape fluctuation typically lowers the measured gradient; thus, the true gradients are likely larger than our estimates.

A second concern arises from optical projection effects, as discussed in the Supplementary Information of Ref.(5) When a spherical tissue has a uniform Ca^{2+} activity, its projected fluorescence image often appears as a ring—initially increasing in intensity from the center before fading toward the perimeter. If the sampling circle shifts away from the image center, a spurious fluorescence gradient can result. However, such shifts are generally random and tend to average out over time. A potential exception occurs when the projected tissue shape narrows on one side and widens on the other, shifting the center of mass and producing a false intensity gradient in the absence of a real polarity cue. In practice, these cases usually coincide with the foot precursor's emergence, at which point we can apply the first method (foot-precursor–

based) that bypasses this artifact. Moreover, in all tested samples where both methods are applicable, they yield consistent fluorescence profiles and indicate the same polarity direction.

Lastly, tissue orientation within the imaging plane can pose a problem. If the true polarity axis is perpendicular to the projection plane, even a substantial Ca^{2+} gradient may appear small. However, this situation again leads to an underestimation rather than a false-positive gradient. Our observations indicate that continuous minor shape fluctuations typically maintain the developing body axis parallel to the imaging plane until later stages of regeneration, when the foot has formed, and the axis may rotate out of focus. This loss of focus serves as an indicator that the tissue is rotating toward a perpendicular orientation.

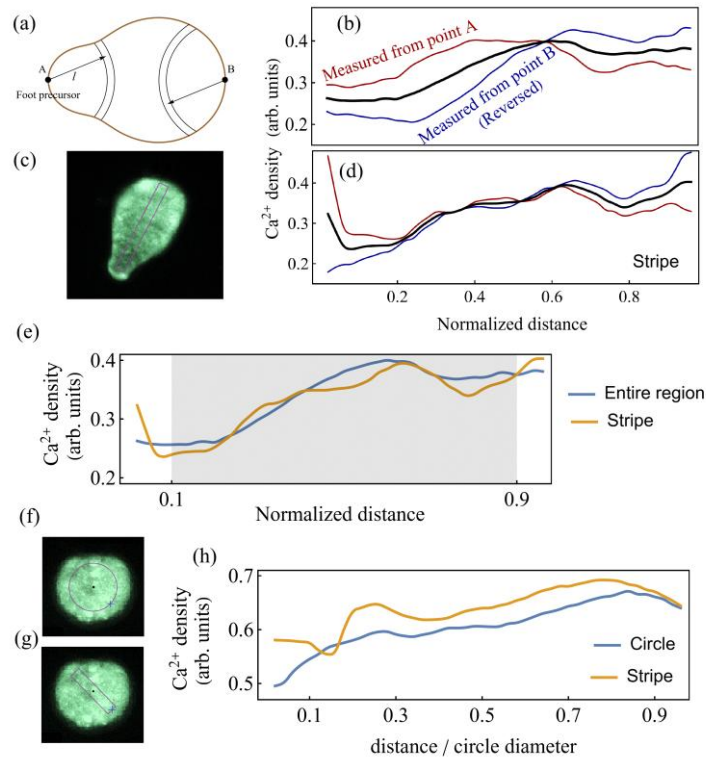


Fig. S8. Computations of the Ca^{2+} Gradient and Validations. (a) Schematic illustration of the definition of the foot precursor's center A and its antipodal point B. (b) Example of the measured Ca^{2+} density (arbitrary units) when averaging over the entire projected region of the tissue (within a polygon of its contour reduced by 10%). Red and blue curves show data measured from A and B, respectively, where the distribution computed from B is flipped. The black curve results from averaging the two sets. Here, distance x is the normalized coordinate along the line connecting A and B. (c) Fluorescence image showing the narrow stripe region (outlined in purple) used to verify that the calculation procedure is robust. (d) Measured Ca^{2+} density restricted to this stripe region. Colors match panel (b): red for A, blue for B (flipped), and black for their average. (e) Comparison of the final averaged density profiles from the entire region (blue) and the stripe (brown). The good agreement in the shaded central region, $0.1 < x < 0.9$, confirms that the gradient calculation accurately captures the Ca^{2+} distribution along A–B. (f) and (g) Fluorescence images illustrating the circular (f) and stripe (g) sampling regions used in the second procedure, which is applied when the tissue is approximately circular and the foot precursor has not yet emerged. (h) An example comparing the measured Ca^{2+} density profiles for the circle (blue) and the stripe (brown). The small difference between these profiles validates the consistency of the second procedure's gradient measurement.

References

1. O. Agam, E. Braun, Hydra morphogenesis as phase-transition dynamics. *EPL* **143**, 27001 (2023).
2. O. Agam, E. Braun, Stochastic morphological swings in *Hydra* regeneration: A manifestation of noisy canalized morphogenesis. *Proceedings of the National Academy of Sciences* **122**, e2415736121 (2025).
3. L. J. P. van der Maaten, G. E. Hinton, Visualizing Data Using t-SNE. *Journal of Machine Learning Research* **9**, 2579–2605 (2008).
4. J. Healy, L. McInnes, Uniform manifold approximation and projection. *Nature Reviews Methods Primers* **4**, 82 (2024).
5. O. Agam, E. Braun, Universal Calcium fluctuations in Hydra morphogenesis. *Phys. Biol.* **20**, 066002 (2023).